Geochimica et Cosmochimica Acta 335 (2022) 56–67

Contents lists available at ScienceDirect

Geochimica et Cosmochimica Acta

journal homepage: www.elsevier.com/locate/gca

Hydrothermal remobilization of subseafloor sulfide mineralization along mid-ocean ridges contributes to the global oceanic zinc isotopic mass balance

Shili Liao [a], Chunhui Tao [a,*], Hanjie Wen [b,i,*], Weifang Yang [a], Jia Liu [c], John W. Jamieson [d], Ágata Alveirinho Dias [e,f], Chuanwei Zhu [g], Jin Liang [a], Wei Li [a], Teng Ding [h], Xiaohu Li [a], Huichao Zhang [h]

[a] Key Laboratory of Submarine Geosciences, Second Institute of Oceanography, Ministry of Natural Resources, Hangzhou 310012, Zhejiang, China
[b] School of Earth Sciences and Resources, Chang'An University, Xi'an 710054, China
[c] Key Laboratory of Geoscience Big Data and Deep Resource of Zhejiang Province, School of Earth Sciences, Zhejiang University, Hangzhou 310027, China
[d] Department of Earth Sciences, Memorial University of Newfoundland, St. John's, NL A1B 3X5, Canada
[e] Institute of Science and Environment, University of Saint Joseph, Macao SAR, China
[f] Instituto Dom Luiz (IDL), Faculdade de Ciências, Universidade de Lisboa, Lisbon, Portugal
[g] State Key Laboratory of Ore Deposit Geochemistry, Institute of Geochemistry, Chinese Academy of Sciences, Guiyang 550081, China
[h] Institute of Marine Geology, College of Oceanography, Hohai University, Nanjing 210098, China
[i] College of Earth and Planetary Sciences, University of Chinese Academy of Sciences, Beijing 100049, China

ARTICLE INFO

Article history:
Received 2 December 2021
Accepted 20 August 2022
Available online 27 August 2022
Associate editor: Tim Conway

Keywords:
Subsurface remobilization
Hydrothermal activity
Mid ocean ridge
Zinc isotopic mass balance

ABSTRACT

Hydrothermal activity on mid-ocean ridges is an important mechanism for the delivery of Zn from the mantle to the surface environment. Zinc isotopic fractionation during hydrothermal activity is mainly controlled by the precipitation of Zn-bearing sulfide minerals, in which isotopically light Zn is preferentially retained in solid phases rather than in solution during mineral precipitation. Thus, seafloor hydrothermal activity is expected to supply isotopically heavy Zn to the ocean. Here, we studied sulfide-rich samples from the Duanqiao-1 hydrothermal field, located on the Southwest Indian Ridge. We report that, at the hand-specimen scale, late-stage conduit sulfide material has lower δ^{66}Zn values (−0.05 ± 0.15 ‰; n = 19) than early-stage material (+0.13 ± 0.15 ‰; n = 10). These lower values correlate with enrichments in Pb, As, Cd, and Ag, and elevated δ^{34}S values. We attribute the low δ^{66}Zn values to the remobilization of earlier sub-seafloor Zn-rich mineralization. Based on endmember mass balance calculations, and an assumption of a fractionation factor ($\alpha_{ZnS\text{-}Sol.}$) of about 0.9997 between sphalerite and its parent solution, the remobilized Zn was found consist of about 1/3 to 2/3 of the total Zn in the fluid that formed the conduit samples. Our study suggests that late-stage subsurface hydrothermal remobilization may release isotopically-light Zn to the ocean, and that this process may be common along mid-ocean ridges, thus increasing the size of the previously identified isotopically light Zn sink in the ocean.
© 2022 Elsevier Ltd. All rights reserved.

1. Introduction

Seafloor hydrothermal activity is an important geological process for the delivery of Zn from the sub-seafloor to the oceans (Tivey, 2007), thus constituting an important part of the global marine Zn cycle and the Zn isotopic balance of the ocean (Isson et al., 2018; John et al., 2018; Roshan et al., 2018). Current studies on the balance of the global oceanic Zn flux have revealed that dissolved Zn in the modern ocean has an isotopically heavy composition (e.g., δ^{66}Zn = +0.46 ± 0.13 ‰; average ± SD; Lemaitre et al., 2020), compared to major Zn inputs (e.g., δ^{66}Zn = +0.33 ‰ for rivers and δ^{66}Zn = +0.37 ± 0.14 ‰ for Aeolian dust; Little et al., 2014). Thus, an isotopically light sink is required to balance the marine Zn budget (Little et al., 2014). A possible candidate was suggested to be the preferential uptake of light Zn in organic-rich continental margin sediments (Little et al., 2016).

Zinc is one of the primary mineral-forming base metals in mid-ocean ridge (MOR) hydrothermal deposits. Significant variations in Zn isotope compositions have been observed in seafloor sulfide mineralization, and these variations have been mainly attributed to the precipitation of minerals that are enriched in isotopically light Zn relative to the fluid (John et al., 2008; Zeng et al., 2021).

* Corresponding authors.
E-mail addresses: taochunhuimail@163.com (C. Tao), wenhanjie@vip.gyig.ac.cn (H. Wen).

https://doi.org/10.1016/j.gca.2022.08.022
0016-7037/© 2022 Elsevier Ltd. All rights reserved.

Thus, due to sub-seafloor mineralizing processes, the fluid becomes continuously more enriched in heavy Zn, and late-stage precipitated minerals from the fluid generally contain heavier Zn than early precipitated minerals. As a result, hydrothermal activity is expected to deliver relatively heavy Zn to the ocean. For example, the highest fluid δ^{66}Zn value was recorded from a low temperature vent fluid at K-vent, a sulfide-rich edifice at EPR 9°N (δ^{66}Zn = +0.98 to +1.04 ‰; John et al., 2008), compared with hydrothermal fluid formed by leaching from MORB that has not undergone subseafloor zinc bearing minerals precipitation (δ^{66}Zn= +0.24 ‰; John et al., 2008). However, because the formation of hydrothermal sulfides on MORs involves multiple processes, such as the contribution of biological activity, multi-stage mixing with seawater and hydrothermal fluids, rapid precipitation of sulfide minerals, and remobilization and re-precipitation of metals from early stage minerals (Tivey, 2007), their Zn isotopic fractionation processes may be more complex, particularly on slow- and ultraslow-spreading ridges that develop deep, steeply dipping, large-scale faults that provide feasible conditions for the formation of deeply circulating, long-lasting, and stable hydrothermal systems (Cherkashov et al., 2017; Grevemeyer et al., 2019). For example, seafloor sulfide deposits contain the largest reported range in Zn isotope compositions (δ^{66}Zn = −0.43 ‰ to +1.24 ‰) among all kinds of mineral deposits, both on land and on the seafloor (Liao et al., 2019). Hydrothermal plumes with negative δ^{66}Zn values were also recorded above the TAG active mound, on the Mid-Atlantic Ridge (−0.5 ‰; Conway and John, 2014), and at a hydrothermal vent of the Reykjanes Ridge (−0.42 ‰; Lemaitre et al., 2020). However, the mechanisms that generate such light Zn isotope compositions in seafloor hydrothermal systems and their influence on the oceanic Zn budget remains unclear.

In this study, we present the Zn isotope compositions of four relict sulfide-rich-mound samples from the Duanqiao-1 hydrothermal field (DHF) on the Southwest Indian Ridge (SWIR; Fig. 1a). We find that late-stage conduit sulfide minerals exhibit isotopically lighter Zn compared with those of early-stage pyrite dominated framework, and propose that this apparent evolution of Zn isotopic compositions results from zone refining processes associated with sub-seafloor mineralization. Our findings suggest that subsurface remobilization may be a common feature during the formation of seafloor sulfide deposits and contributes to the global oceanic Zn isotopic mass balance.

2. Geological background and sample description

The study area is located on segment 27 of the ultraslow-spreading SWIR (half-spreading rate of 0.7–0.9 cm/yr, Dick et al., 2003) between the Indomed and Gallina transfer faults. Geophysical surveys have revealed that the morphology, crustal thickness, mantle composition, and magma activity vary along the ridge axis (Georgen et al., 2001; Sauter et al., 2009). In segment 27, the volcanic ridge axis is well developed without an apparent rift valley (Fig. 1b). This segment features a ~9.5 km thick oceanic crust (Li et al., 2015) and a well-developed magma chamber (Jian et al., 2017), although the origin of the magma chamber is controversial (e.g., associated with the Crozet hotspot, local magmatic conditions, or regional mantle fertility driven by plate reorganization; Yang et al., 2017; Yu and Dick, 2020).

The DHF, located on the ridge axial high at a depth of about 1,700 m, was discovered by deep-tow video imaging in 2008 during the DY115-20 Cruise, and consists of a sulfide-rich mound covering a 200 × 125 m area (Tao et al., 2012). Massive sulfide rubble and chimney fragments are distributed on the surface or adjacent to the mound. Abundant opal was found covering the center of the mound. The host rocks of the mineralization are basalts and basaltic breccias, and sediments are distributed along the slopes or in topographic depressions. Massive sulfide outcrop, sulfide debris, and opal samples were collected using a TV-grab system consisting of a cable-based vertical sampling tool equipped with a live-feed camera. During tow-yo or CTD station investigations, no turbidity, temperature, or methane anomalies were detected (Tao et al., 2014).

Four sulfide-rich relic samples exhibiting mineral zonation were collected from the sulfide mound for Zn isotopic analysis. The main constituents of the studied samples are a pyrite-dominated framework, that is overgrown and/or replaced by

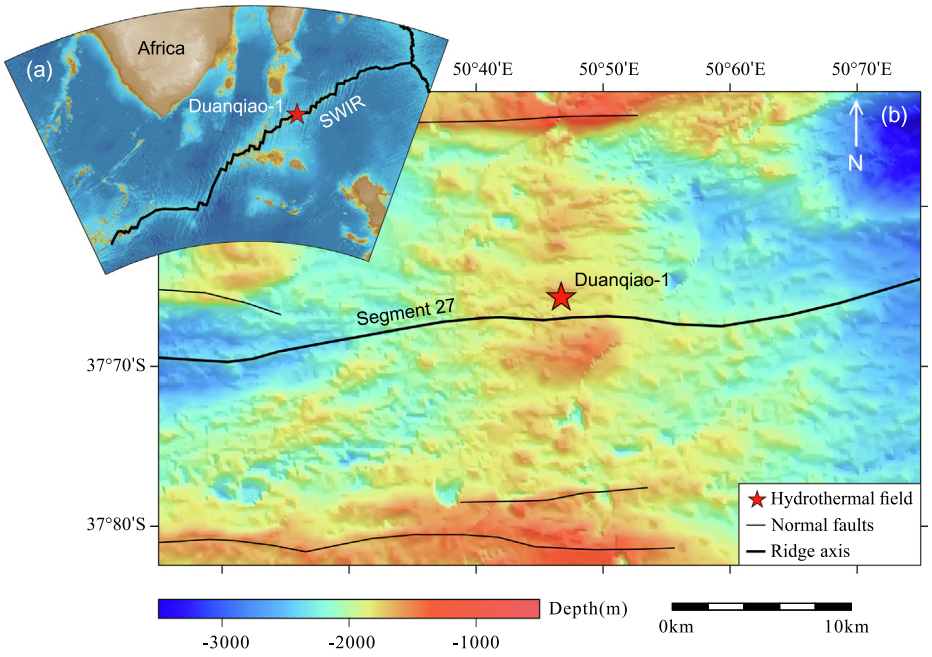

Fig. 1. (a) Location and (b) bathymetry of the study area. The bathymetric data for (a) and (b) were obtained from General Bathymetric Chart of the Oceans (Schenke, 2016) and multibeam bathymetry survey, respectively.

late-stage conduit minerals comprising chalcopyrite, sphalerite, and opal. The late-stage conduits are divided into chalcopyrite-dominated (Fig. 2a and b), sphalerite-dominated (Fig. 2c), and opal-dominated (Fig. 2d), with the different primary minerals reflecting variable formation temperatures. These conduit minerals also occur in minor abundances within the pyrite-dominated framework. At a hand specimen scale, the contact zone between the framework and conduit minerals is distinct, with obvious overgrowth features. Dating results using $^{230}Th/^{238}U$ ratios indicate that these samples may have been formed through a minimum of four episodes of hydrothermal activity between 0.7 and 84.3 kyrs (Yang et al., 2016).

The pyrite-dominated framework mainly comprises anhedral pyrite with minor marcasite (Fig. 3a). The chalcopyrite-dominated conduit is primarily composed of anhedral to euhedral chalcopyrite, sphalerite, and minor pyrite. In the conduit walls, original euhedral pyrite was replaced by chalcopyrite (Fig. 3b), which was subsequently replaced by sphalerite (Fig. 3c). Occasionally, inner conduit walls are dominated by sphalerite or opal, suggesting the sphalerite and opal-dominated conduits were formed after chalcopyrite dominated conduits. Sphalerite-dominated conduit walls comprise sphalerite and anhedral pyrite (Fig. 3d and e), with minor chalcopyrite. Opal-dominated conduits comprise high contents of silica, and the conduit walls are mainly composed of quartz, sphalerite, pyrite, and minor tetrahedrite (Fig. 3f).

3. Methods

3.1. Microdrilling

Microdrilling (Microdrill System) was conducted at the State Key Laboratory of Ore Deposit Geochemistry, Institute of Geochemistry, Chinese Academy of Sciences. This instrument conducts in situ sampling during optical observations to ensure the purity of each collected sample. The diameter of the micro drill bit ranges from 0.2 to 2 mm. To obtain pure samples, a vacuum adsorption system was used to collect the drilled material. The sampling methods and specific parameters for this instrument have been previously described (Dong et al., 2013).

3.2. Sulfur isotopes

Sulfur isotope ratios of the microdrilling samples were measured at the State Key Laboratory of Ore Deposit Geochemistry. <100 μg of sulfide material was combusted in a tin cup using a Flash EA 2000 elemental analyzer attached to an isotope ratio mass spectrometer (Thermo Finnigan MAT 253; Thermo Scientific, Bremen, Germany). The International Measurement Standard reference materials IAEA-S-1 (Ag_2S reference material 8554), IAEA-S-2 (reference material 8555), and IAEA-S-3 (reference material 8529) yielded a relative error of <0.15 ‰ (n = 10). The S isotope ratios are reported relative to Canyon Diablo Troilite using standard delta notation, where $\delta^{34}S = [(^{34}S/^{32}S)_{sample}/(^{34}S/^{32}S)_{CDT} - 1] \times 1000$.

3.3. Zinc isotopes

For zinc isotope analyses, the micro drilled samples were first weighed and digested in Teflon digestion vials (Savilex; USA) using 1 mL concentrated HNO_3 and 0.1 mL concentrated HF at 110 °C for approximately 24 h. After drying, the samples were dissolved in 5 mL of 1 % HNO_3 (v/v%). For each sample, 2 mL of supernatant solution was transferred into a 15 mL polypropylene centrifuge tube for trace element analysis. The residuals were evaporated to

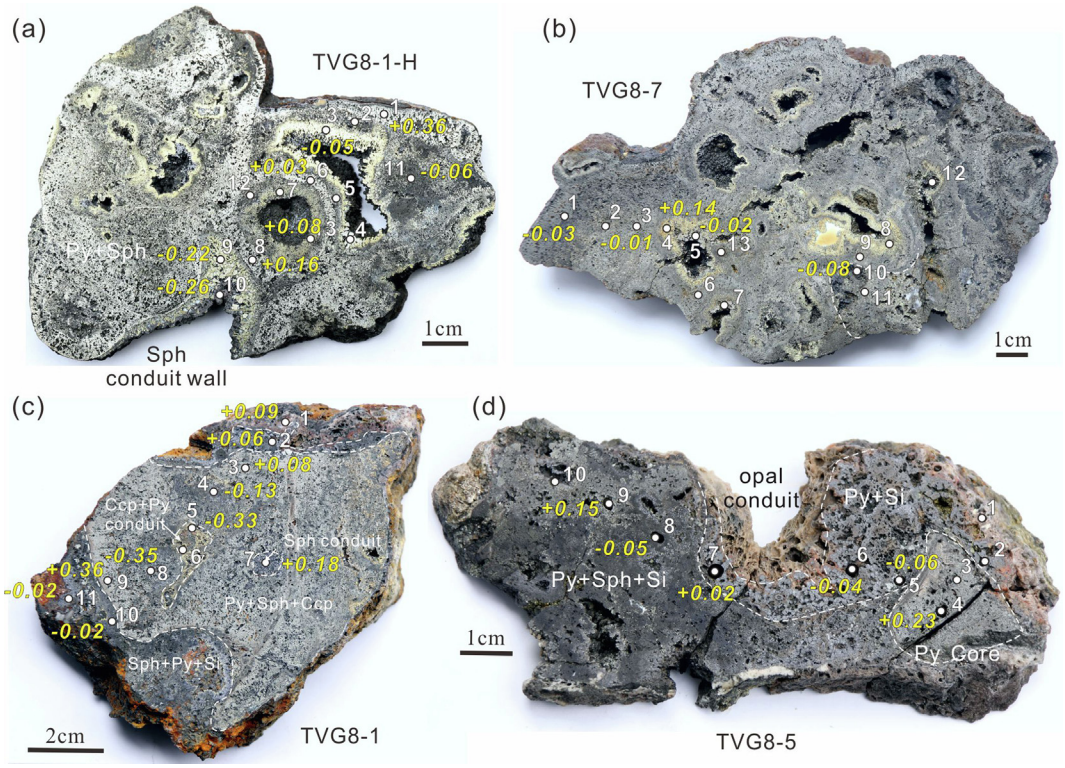

Fig. 2. Sulfide mound relict samples selected in this study. These samples show distinct and obvious overgrowth features between the conduit and framework (most evident in a, c, and d), implying the early-stage debris were cemented by late stage sulfide. The microdrilling sample positions and sample numbers are represented by the white dots and numbers, and the analyzed Zn isotope composition (‰) are represented by the yellow italic numbers. (a) Pyrite-rich framework replaced by chalcopyrite-rich conduit, (b) pyrite-rich framework replaced by chalcopyrite-rich conduit, (c) pyrite-rich framework replaced by sphalerite- and chalcopyrite-rich conduits and sphalerite-silicon rich veins, and (d) pyrite-silicon rich conduit developing opal and pyrite on the inner and outer walls of the conduits, respectively.

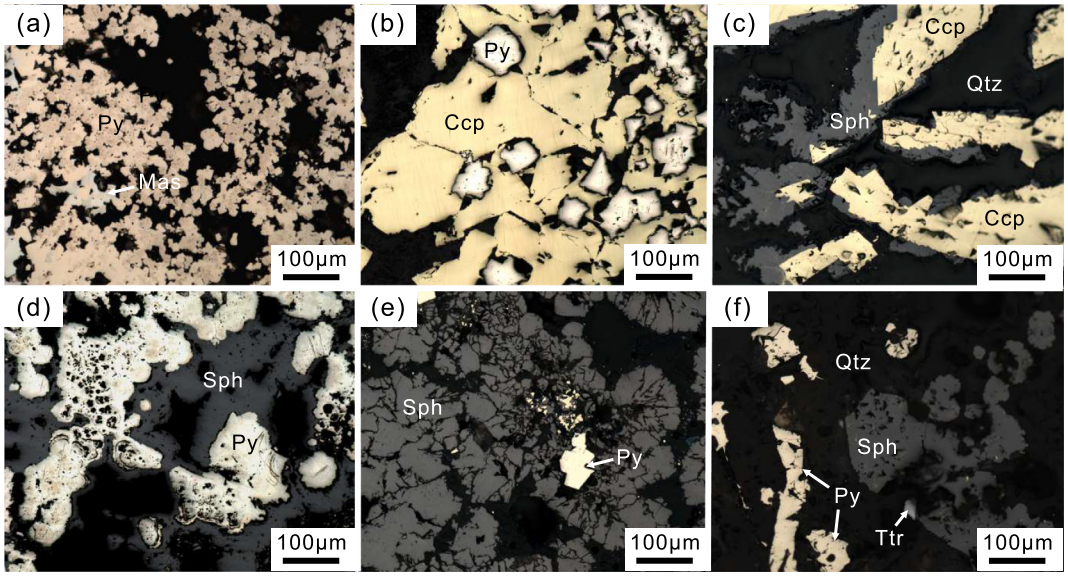

Fig. 3. Photomicrographs of the studied sulfides. (a) Anhedral pyrite intergrown with marcasite in the pyrite-dominated framework, (b) chalcopyrite replacing euhedral pyrite in the chalcopyrite-dominated conduit, (c) sphalerite overgrown with chalcopyrite in the conduit, (d) sphalerite replacing pyrite in the conduit, (e) sphalerite in the conduit, and (f) sphalerite and pyrite intergrown with quartz in the opal-dominated conduit. Mineral abbreviations: Ccp, chalcopyrite; Mas, marcasite; Py, pyrite; Sph, sphalerite; Ttr, tetrahedrite; Qtz, quartz.

dryness and then dissolved using 2 mL 2 M HCl for the Zn isotope separation. Trace element concentrations were determined by inductively coupled plasma optical emission (ICP-OES) at the ALS Laboratory Group, Guangzhou, China. The Zn isotope aliquots were chemically purified by pre-cleaned 100–200 mesh AG MP-1 M anion-exchange resin. The method for purification is described by Liao et al. (2019). The comparison of zinc content of unprocessed and purified samples indicated > 99 % recovery of Zn.

Zinc isotope analyses were performed by multi-collector inductively coupled plasma mass spectrometry (MC-ICP-MS) (Neptune plus) at the State Key Laboratory of Crust–Mantle Evolution and Mineralization, Nanjing University. A coupled method of sample-standard bracketing and Cu-doping was used for correction of instrumental mass bias of the Zn isotopes (Wang et al., 2015), and Faraday cups were aligned to measure ^{63}Cu (L3), ^{64}Zn (L2), ^{65}Cu (L1), ^{66}Zn (center cup), ^{67}Zn (H1), ^{68}Zn (H2), and ^{70}Zn (H4) isotopes. The Cu and Zn concentrations of the samples and standards (reference material ERM-AE633) were diluted to 0.5 μg/g and 1.0 μg/g, respectively (Zhu et al., 2018). Zn isotope ratios were analyzed in low-resolution mode with a combination of Ni Standard sampler cone and Ni X-type skimmer cone. The samples and standards were both introduced into the mass spectrometer using a Teflon nebulizer and spray chamber at an uptake rate of about 100 μL/min, and generally ranged at a total Zn voltage of 30 V/ppm. All the samples and standard solutions were analyzed in three blocks, with 15 cycles per block.

The Zn isotopic ratios are expressed in standard delta notation in per mil units relative to the Institute for Reference Materials and Measurements (IRMM) 3702a Zn solution. The Zn isotope composition was represented as $\delta^{66}Zn = [(^{66}Zn/^{64}Zn)_{sample}/(^{66}Zn/^{64}Zn)_{IRMM\text{-}3702a} - 1] \times 1000$. CAGS-1 and the new AA-ETH Zn isotope standard solutions were used as internal laboratory secondary reference materials; the $\delta^{66}Zn_{IRMM\ 3702}$ values of which were −0.85 ± 0.05 ‰ (n = 6) and −0.01 ± 0.05 ‰ (n = 6), respectively, in which the AA-ETH value agreed well with previous reported values (Archer et al., 2017). An international sulfide standard (J-Zn-1) was used as an internal laboratory solid standard to monitor Zn isotope fractionation during Zn purification and isotope analysis; the $\delta^{66}Zn_{IRMM\ 3702}$ value of J-Zn-1 was −0.08 ± 0.05 ‰, which was in alignment with published values (Yang et al., 2022a). To compare this study to literature data, the Zn isotopic data are converted to the JMC Zn isotope standard by the following equation: $\delta^{66}Zn_{JMC} = \delta^{66}Zn_{IRMM\ 3702} + 0.29$ (Wang et al., 2017).

4. Results

Zinc and S isotope compositions and trace element ratios of selected Duanqiao-1 samples are listed in Table 1. Location of micro drilling samples collected for analyses are provided in Fig. 2. Because of the unknown mass of the micro drilled samples, the trace element concentrations are reported as ratios. The samples exhibit $\delta^{66}Zn$ values ranging between −0.35 ‰ and +0.36 ‰, with the early-stage pyrite-dominated framework samples showing heavier Zn (−0.05 ‰ to +0.36 ‰; average ± SD = 0.13 ± 0.15 ‰; n = 10) than the late-stage conduit wall sulfides (range of −0.35 ‰ to +0.18 ‰; average of −0.05 ± 0.15 ‰; n = 19) (Fig. 4a). The range of the $\delta^{66}Zn$ values are consistent with current seafloor sulfide observations (Fig. 4b). Most of the values were lower than those of the host basaltic rocks (+0.28 ± 0.03 ‰; Wang et al., 2017), which is in agreement with a process whereby hydrothermal alteration of basalt preferentially releases light Zn into the hydrothermal fluid (Huang et al., 2016). However, the conduit-wall exhibited generally comparable but slightly increased $\delta^{66}Zn$ values from Cu-rich (−0.09 ± 0.18 ‰, n = 7), to Zn-rich (−0.05 ± 0.17 ‰, n = 7), and to opal-dominated samples (−0.01 ± 0.07 ‰, n = 5, respectively, Fig. 4a).

5. Discussion

5.1. Mineralogical controls on the occurrence of Zn

Petrographic observations reveal that the DHF samples are mainly composed of pyrite, sphalerite, and chalcopyrite, with minor tetrahedrite and marcasite (Fig. 3). Sphalerite is therefore the dominant Zn-bearing mineral phase in these samples. Thus, the Zn isotope compositions of the Zn-rich samples (e.g. the sphalerite dominated conduits) is expected to be largely controlled by sphalerite. However, hydrothermal pyrite can also have a high Zn

Table 1
Zinc, S isotope compositions and representing trace element ratios of the studied sulfide samples from Duanqiao-1.

Sample	Serie No.	Description	$\delta^{34}S$ (‰V_{CDT})	$\delta^{66}Zn_{JMC}$ (‰)	2SD	Zn/Cd	Zn/Cu	Zn/Fe	Co/Ni	As/Ni	Ag/Ni	Cd/Ni	As/(Cu+ Zn + Fe)	Ag/(Cu+ Zn + Fe)	Cd/(Cu+ Zn + Fe)	Pb/(Cu+ Zn + Fe)
TVG08-1H	1	Py dominated framework	+3.95	+0.36	0.03	818.0	20.14	0.15	1.00	7.00	3.20	1.00	11.38	5.20	1.63	69.92
	2	Py dominated framework	+5.05	–	–	–	–	–	–	–	–	–	–	–	–	–
	3	Ccp dominated conduit	+4.96	−0.05	0.01	133.8	0.02	0.02	–	–	–	–	1.48	3.10	0.74	–
	4	Ccp-Py dominated conduit	+2.42	–	–	–	–	–	–	–	–	–	–	–	–	–
	5	Sph dominated conduit	+4.42	–	–	–	–	–	–	–	–	–	–	–	–	–
	6	Py dominated framework	+4.30	+0.03	0.01	–	0.16	0.02	3.00	11.00	0.90	–	19.15	1.57	–	22.63
	7	Ccp-Py dominated conduit	+4.94	–	–	–	–	–	–	–	–	–	–	–	–	–
	8	Py dominated framework	+3.95	+0.16	0.02	201.5	1.18	0.05	1.33	5.00	0.27	0.67	15.70	0.84	2.09	39.77
	9	Ccp-Py dominated conduit	+4.90	−0.22	0.04	354.4	2.58	0.08	1.50	5.50	0.35	1.00	11.49	0.73	2.09	36.56
	10	Ccp-Sph dominated conduit	+5.74	−0.26	0.04	177.3	0.10	0.06	2.50	7.00	3.15	2.00	7.19	3.24	2.06	1.03
	11	Sph dominated conduit	+5.15	−0.06	0.03	213.1	6.42	0.25	2.00	5.50	0.98	2.00	24.69	4.38	8.98	21.32
	12	Sph dominated conduit	+4.58	–	–	–	–	–	–	–	–	–	–	–	–	–
	13	Ccp-Py dominated conduit	+5.04	+0.08	0.01	–	0.06	0.02	–	–	–	–	8.91	1.34	–	13.36
TVG08-7	1	Py-Sph dominated framework	+4.65	−0.03	0.04	152.2	47.49	0.82	0.09	0.79	0.19	2.82	8.18	1.98	29.24	35.85
	2	Py dominated framework	+4.67	–	–	–	–	–	–	–	–	–	–	–	–	–
	3	Py dominated framework	+4.36	−0.01	0.01	133.5	1.44	0.13	0.17	0.57	0.12	0.29	16.44	3.37	8.22	32.88
	4	Ccp dominated conduit	+5.12	+0.14	–	–	0.01	0.06	0.50	–	1.00	–	–	3.06	–	–
	5	Ccp-Py dominated conduit	+4.82	−0.02	0.01	145.7	1.04	0.25	23.00	83.00	8.30	58.00	16.28	1.63	11.37	7.26
	6	Py dominated framework	+4.69	–	–	–	–	–	–	–	–	–	–	–	–	–
	7	Ccp-Py dominated conduit	+3.84	–	–	–	–	–	–	–	–	–	–	–	–	–
	8	Ccp dominated conduit	+5.01	–	–	–	0.01	0.01	0.60	0.40	0.42	–	0.81	0.85	–	–
	9	Py dominated framework	+5.29	–	–	–	–	–	–	–	–	–	–	–	–	–
	10	Opal-Py dominated conduit	+5.08	−0.08	0.02	18.4	2.01	0.86	0.33	0.17	0.98	7.33	4.66	27.47	204.84	111.73
	11	Py dominated framework	+4.60	–	–	–	–	–	–	–	–	–	–	–	–	–
	12	Sph dominated conduit	+4.99	–	–	–	–	–	–	–	–	–	–	–	–	–
	13	Py dominated framework	+4.78	–	–	–	–	–	–	–	–	–	–	–	–	–
TVG08-1	1	Opal dominated conduit	–	+0.09	0.04	–	0.56	0.59	0.14	0.36	–	–	463.95	–	–	278.37
	2	Sph dominated conduit	+6.11	+0.06	–	308.5	56.48	20.89	–	–	–	–	9.36	4.45	30.42	266.79
	3	Py dominated framework	+4.50	+0.08	0.03	251.0	0.87	0.04	0.50	1.00	0.20	0.17	9.65	1.93	1.61	32.16
	4	Sph dominated conduit	+4.70	−0.13	0.03	14.4	1.12	0.28	0.67	1.33	1.03	10.00	17.10	13.26	128.29	8.55
	5	Ccp dominated conduit	+4.87	−0.33	0.01	122.8	0.24	0.11	2.50	4.00	2.00	2.50	9.04	4.52	5.65	5.65
	6	Ccp dominated conduit	+4.81	–	–	–	–	–	–	–	–	–	–	–	–	–
	7	Sph-Py dominated conduit framework contaminated	+5.22	+0.18	–	37.0	2.99	1.14	0.50	–	2.50	13.50	–	22.59	122.01	266.61
	8	Sph dominated conduit	+4.26	−0.35	0.05	152.9	18.54	0.45	1.50	4.00	1.15	6.00	13.35	3.84	20.02	23.36
	9	Py dominated framework	+3.79	+0.36	0.04	214.6	5.80	0.03	1.00	5.50	1.15	0.50	17.21	3.60	1.56	26.60
	10	Sph dominated conduit	+5.35	−0.02	0.01	200.6	25.07	1.30	1.00	3.00	5.60	18.00	4.60	8.58	27.59	27.59
	11	Sph dominated conduit	+6.33	−0.02	–	204.7	21.29	4.29	–	–	–	–	3.47	4.16	38.16	28.62
TVG08-05	1	Opal-Py dominated conduit	+7.97	–	–	–	–	–	–	–	–	–	–	–	–	–
	2	Opal-Py dominated conduit	+6.65	–	–	–	–	–	–	–	–	–	–	–	–	–
	3	Py dominated framework	+4.42	–	–	–	0.53	0.02	–	–	–	–	–	–	–	–
	4	Py dominated framework	+4.59	+0.23	0.09	–	1.35	0.02	0.08	0.77	0.16	–	17.23	3.62	–	74.07
	5	Opal-Py dominated conduit	+5.44	−0.06	0.04	150.0	7.50	0.30	0.50	2.00	1.60	3.50	8.49	6.79	14.86	33.97
	6	Opal-Py dominated conduit	+6.53	−0.04	0.04	23.9	9.20	0.93	–	1.00	0.66	20.20	9.52	6.28	192.28	26.65
	7	Opal-Py dominated conduit	+6.74	+0.02	0.02	–	166.18	19.48	–	1.00	2.60	25.00	1.67	4.35	41.85	17.58
	8	Py-opal dominated framework	+4.71	−0.05	0.02	226.0	3.09	1.25	–	0.75	2.03	2.25	8.63	23.31	25.90	57.56
	9	Py-opal dominated framework	+4.83	+0.15	0.01	181.7	1.32	0.05	–	1.33	0.43	0.17	15.63	5.08	1.95	25.40
	10	Py-opal dominated framework	+6.06	–	–	225.7	–	–	–	–	–	–	–	–	–	–

Note: - represents no data. $\delta^{34}S$ data of samples TVG08-1H and TVG08-05 were from Yang et al., 2022b. The serial numbers correspond to the positions of the micro drilling samples were shown in Fig. 2. The ratios of As, Ag, Cd and Pb to Cu + Zn + Fe were presented in × 10^4. Typical SD on $\delta^{34}S$ was <0.15 ‰.

content (up to 15,000 μg/g, Keith et al., 2016) in the form of microparticle sphalerite inclusions (Reich et al., 2013). With the exception of two samples with Zn/Fe of 0.82 and 1.25, the pyrite-dominated framework samples have Zn/Fe between 0.02 and 0.15 (average: 0.06 ± 0.05; n = 9), lower than the highest Zn/Fe ratio obtained by an electron probe micro-analyzer (ranging from 0.0 to 1,820.8 × 10^{-4}; 323.7 × 10^{-4} ± 471.1 × 10^{-4}; n = 16, Zhang et al., 2018). As a result of the limited spot diameter and by deliberately avoiding micro inclusions, these high Zn/Fe values obtained by EPMA reflect Zn substitution of Fe in the pyrite, indicating that Zn isotope compositions reflect Zn in both pyrite and sphalerite in pyrite-dominated framework samples. The Zn/Cu ratios in the chalcopyrite from the DHF samples exhibited significantly lower values (0.02 to 0.10 × 10^{-4}; 0.03 ± 0.02 × 10^{-4}; n = 15, Zhang et al., 2018) than those of our bulk samples (0.51 ± 0.91; n = 8). Chalcopyrite is a relatively poor carrier of Zn (George et al., 2018), and the Zn isotopic composition of the chalcopyrite-dominated conduit samples likely reflect the Zn in sphalerite. The opal-dominated conduit samples also show high Zn/Fe and Zn/Cu ratios (0.30–19.48, and 0.56–166.18, respectively, n = 5) that are comparable with that of sphalerite dominated conduit samples (0.25–20.89, and 1.12–25.07, respectively, n = 7), but significantly higher than that of pyrite-dominated framework samples. This observation suggests that their Zn isotope composition was also predominantly reflecting Zn in the sphalerite.

5.2. Zn isotope systematics

The sampled late-stage conduit minerals (δ^{66}Zn = −0.05 ± 0.15 ‰; n = 19) contain isotopically light Zn compared to those of the early-stage pyrite-dominated framework samples (0.13 ± 0.15 ‰; n = 10). In addition, among the late-stage conduit samples, the inner chalcopyrite-dominated and the sphalerite- and opal-dominated conduit samples have generally comparable δ^{66}Zn values (Fig. 4a). These results indicate decreasing δ^{66}Zn values with time during the formation of these samples. Case studies and *Ab initio* simulations of mineral deposits indicate that lighter Zn isotopes preferentially fractionate into the precipitating solid phase relative to the mineralizing solution under low P_{CO2} conditions (Kelley et al., 2009; Fujii et al., 2011; Zhou et al., 2014). For example, the predicted fractionation between sphalerite and associated fluid is <−0.25 ‰ at 423 K and under low P_{CO2} conditions (Fujii et al., 2011). Therefore, after sphalerite precipitation, the residual hydrothermal fluids are assumed to be enriched in heavy Zn, and any subsequent sulfide mineral precipitation from these fluids should contain relatively heavier Zn than the earlier precipitated sphalerite. To our knowledge, this is the first time that this reversed evolution of Zn isotope composition has been documented at the hand-specimen scale in seafloor sulfide samples. Therefore, we suggest that another source of light Zn must be added during the mineralization process to produce later stage Zn-bearing minerals with light δ^{66}Zn signatures.

The mixing of Zn isotope compositions from deep seawater, deep-sea sediments, and biogenic opal as a source of light Zn can be excluded, due to the late-stage conduit sulfide samples exhibiting lighter δ^{66}Zn distributions than these potential sources (Fig. 4b; Liao et al., 2019 and references therein). The possible influx of a bacterially-derived isotopically light Zn source can also be excluded because the high temperature conditions in the reaction zone inhibit bacterial activity (Sarrazin et al., 1999), and the S isotope data are inconsistent with bacterial derived signals (see below). In addition, it has been proposed that high temperature fluids that have not precipitated subsurface Zn-bearing minerals would exhibit comparable Zn isotope compositions to source rocks (John et al., 2008). For example, measurements of active vent fluids from Bio" 9 vent from the 9°N East Pacific Rise have revealed that high-temperature (>300 °C) hydrothermal fluids have δ^{66}Zn values (+0.24 ‰; John et al., 2008) similar to those of MORB (+0.28 ± 0.03 ‰; Wang et al., 2017). However, the δ^{66}Zn values of the chalcopyrite-dominated conduit sulfide samples in our study yielded a wide distribution range (δ^{66}Zn value −0.33 ‰ to +0.14 ‰), with the lowest value being significantly lower than that of MORB (Wang et al., 2017). Furthermore, although preferential scavenging of heavy Zn by solids, such as oxyhydroxides, clay minerals formed by wall rock alteration, and organic compounds can result in precipitates with low δ^{66}Zn values (Liu et al., 2019; Chen et al., 2014), the high sphalerite content of the conduit samples implies that zinc was not significantly absorbed, thus making this process unlikely to be important at high-temperature hydrothermal vents.

We propose instead that the light Zn of the late-stage conduit samples is caused by the remobilization of early-stage subsurface mineralization. This interpretation is supported by the studied conduit samples exhibiting relatively high concentrations of hydrothermally mobile elements (e.g., Ag and Cd) but lower concentrations of immobile elements (e.g., Ni), compared to the early-stage framework samples (Fig. 5a and b). The Ag, As, Pb, and Cd contents of the conduit samples are also high compared to other hydrothermal sites on the SWIR and other mafic and ultramafic hosted sites on sediment-starved mid-ocean ridges (Fig. 5c and d; Yang et al., 2022b). However, the elevated values are comparable to sulfide minerals from white smokers on the surface of the active TAG mound, where venting fluids are also hypothesized to have been modified by the dissolution of earlier stage subsurface Zn sulfide minerals (Tivey et al., 1995). This interpretation is also consistent with the remobilized and reprecipitated sulfide mineralization (mainly comprise secondary sphalerite and chalcopyrite) of the Alexandrinka volcanogenic massive sulfide deposit, which exhibits significantly lower δ^{66}Zn values (−0.30 ‰ to −0.05 ‰) than those of associated sulfide chimneys (−0.02 ‰ to +0.23 ‰; Mason et al., 2005).

The interpretation of remobilization of early-stage subsurface mineralization is also supported by the results of S isotope analyzes. The δ^{34}S values of the samples exhibit a reversed evolutionary trend relative to the δ^{66}Zn values (Fig. 4a and c, Fig. 6a), where the late-stage conduit samples generally exhibited heavier S (δ^{34}S = +5.21 ± 1.03 ‰; n = 28) but lighter Zn isotope compositions (δ^{66}Zn = −0.05 ± 0.15 ‰; n = 19) than those of the early-stage pyrite-dominated framework samples (δ^{34}S = +4.62 ± 0.52 ‰; n = 18 and δ^{66}Zn = +0.13 ± 0.15 ‰; n = 10). At the hand-specimen scale, the δ^{34}S values of most of the conduit samples were observed to be 1 ‰–2‰ higher than the framework samples, with the largest difference (+3.55 ‰) observed in sample TVG08-5 (Table 1). Generally, the S isotope compositions of sulfide minerals in sediment-starved MORs are mainly derived from basement rocks (δ^{34}S = +0.1 ± 0.5 ‰) and seawater (δ^{34}S = +21.24 ‰; Tostevin et al., 2014). The increased δ^{34}S values of the samples probably resulted from the presence of different proportions of mixed endmembers controlled by permeability variations of the sulfide. However, such increased δ^{34}S values could also have been caused by the metasomatism of early sulfate minerals, changes of S isotopic composition of the H_2S by deep water–rock reactions, or local S isotopic disequilibrium during sulfide deposition (Zeng et al., 2017 and references therein).

In our studied samples, the enrichment of ^{34}S in the conduit samples caused by variations in permeability of the sulfide structures can be excluded, because these effects would likely equally cause variations in the framework samples. In addition, recent experimental and theoretical studies have demonstrated that deposited sulfide minerals exhibit minor different S isotope compositions compared to the parent fluid, with greater differences exhibited under lower temperatures and longer times for

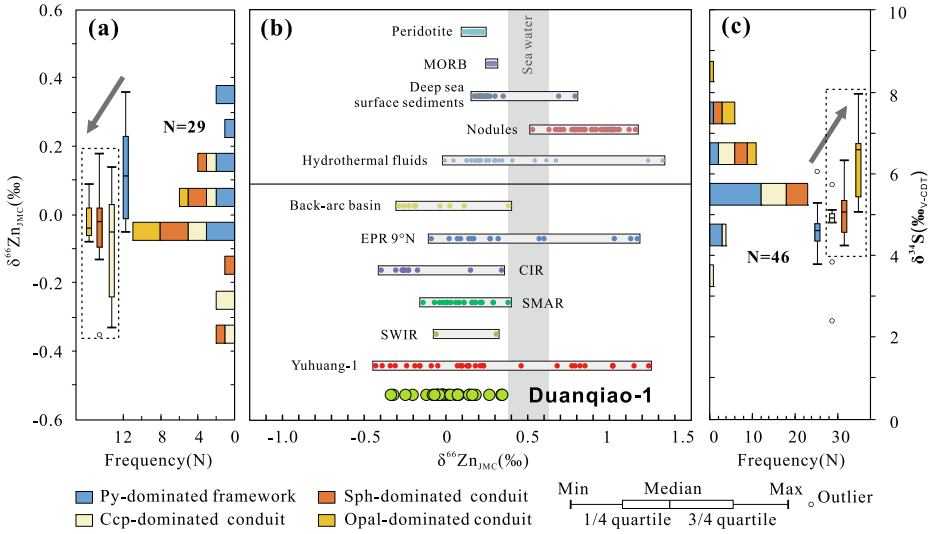

Fig. 4. (a) Histogram of the Zn isotope composition frequency, and (b) a comparison of Duanqiao-1 with sulfide-rich samples from other seafloor hydrothermal fields and potential sources; (c) Histogram of the S isotope composition frequency of the studied samples. Data base: Liao et al. (2019), Zhang et al. (2019), Zeng et al. (2021) and references therein.

equilibration (Ohmoto, 1972; Syverson et al., 2015). Equilibration times within hydrothermal vents are generally very short, and thus the sulfur isotope differences observed in this study cannot be formed by this mechanism. In addition, the pyrite dominated framework and the conduits were formed during different episodes of hydrothermal activities (Yang et al., 2016), which is also inconsistent with this explanation. Furthermore, the Zn/Cd ratio exhibits a low correlation with the $\delta^{34}S$ values in our samples (Fig. 6b), implying that temperature had limited impact on the sulfur fractionation. The isomorphous substitution of Cd for Zn in sphalerite is generally temperature dependent. Sphalerites in ore deposits formed under higher temperatures have higher Cd contents and lower Zn/Cd ratios than lower-temperature sphalerites (Schwartz, 2000; Wen et al., 2016). Therefore, we propose that the high $\delta^{34}S$ values of the conduit samples can be attributed to intermittent hydrothermal activity, which is supported by the framework and conduit samples having been formed during different episodes of hydrothermal activity (Yang et al., 2016). The root of the hydrothermal system would have been filled with seawater during inactive periods, which could have supplied greater amounts of S from seawater to the following re-activated stages of mineralization (Petersen et al., 2000), thus increasing the $\delta^{34}S$ values. In addition, the reduction of the hydrothermal fluid flux during the waning stage of the hydrothermal activity may also result in increasing seawater derived sulfur forming the conduits.

5.3. The extent of subseafloor remobilization

As discussed above, the conduit sulfide samples are products of a sub-seafloor zone refining process. Therefore, the isotopic composition of Zn of the fluid that forms such products can be estimated by an endmember mass balance calculation. The final-stage fluids that form the conduit samples are considered a mixture of the initial fluid, the leachate (remobilized fluid), and seawater. The initial fluid was derived from leaching from host rocks, while the leachate is considered as leaching from earlier precipitated minerals.

The initial fluids should have an S isotope composition slightly higher than the host rocks ($\delta^{34}S$ = +0.1 ‰), due to the incorporation of S derived from thermochemical sulfate reduction in the downwelling fluids. Herein, a $\delta^{34}S_{initial\ fluid}$ value of +1.0 ‰ to +1.5 ‰ is assumed, based on typical $\delta^{34}S$ values of H_2S in the reaction zone released into the hydrothermal system (+1.0 ‰ to +1.5 ‰; Shanks and Seyfried Jr, 1987; Woodruff and Shanks, 1988; Shanks, 2001). The Zn isotopic compositions of the initial fluids are assumed to be similar to high temperature vent fluids (Huang et al., 2016) due to minimal Zn-bearing mineral precipitation. Here, we assume that the $\delta^{66}Zn_{initial\ fluid}$ value is about +0.24 ‰, based on the measured values of high temperature vent fluids at Bio 9, EPR 9°50′N that are assumed to vent without significant sub-seafloor precipitation of Zn bearing minerals (John et al., 2008).

The remobilized fluid is presumed to contain a component of Zn that was leached from a source likely between the initial precipitated sub-seafloor sulfide minerals and the pyrite dominated framework. According to a fractionation factor ($\alpha_{ZnS\text{-}Sol.}$) of about 0.9997 between sphalerite and the parent solution (Fujii et al., 2011; Jamieson-Hanes et al., 2017), the initial precipitated sphalerite should exhibit a range of values that average at a slightly heavier value than the minimum (−0.05 ‰), and would have the lowest $\delta^{66}Zn_{initial\ precipitates}$ values of about −0.03 ‰, assuming 0 % to 20 % of Zn has precipitated from the fluid (Fig. 7). Hence, the hydrothermal fluid from the remobilization of primary Zn bearing minerals (such as sphalerite) would have a Zn isotope composition comparable to the initially deposited sphalerite (−0.05 ‰; Fernandez and Borrok, 2009), or comparable to the pyrite-dominated framework (average $\delta^{66}Zn$ = +0.13 ‰). Thus, the $\delta^{66}Zn_{leachate}$ values are presumed to be between −0.05 ‰ and +0.13 ‰. Subsurface mineralization generally occurs at high temperatures, while there is limited equilibrium S isotope fractionation between H_2S and sulfide minerals under temperatures of ≥250 °C (Ohmoto, 1979). Therefore, the $\delta^{34}S$ values of precipitated sulfide minerals likely reflect the isotopic composition of the parent hydrothermal fluids (Bluth and Ohmoto, 1988). Thus, the S isotope composition of the leachate of the subsurface sphalerite is presumed to be comparable to the isotopic composition of the pyrite-dominated framework (average $\delta^{34}S_{leachate}$ = +4.62 ‰).

Infiltrating seawater into the hydrothermal system has an isotopic composition of $\delta^{66}Zn_{\ Seawater}$ = +0.46 ‰ (Lemaitre et al., 2020) and $\delta^{34}S_{\ Seawater}$ = +21.24 ‰ (Tostevin et al., 2014). The final mixed fluid is presumed to have a $\delta^{34}S_{final\ fluid}$ value similar to the precipitated chalcopyrite-rich conduit samples (average $\delta^{34}S$ =

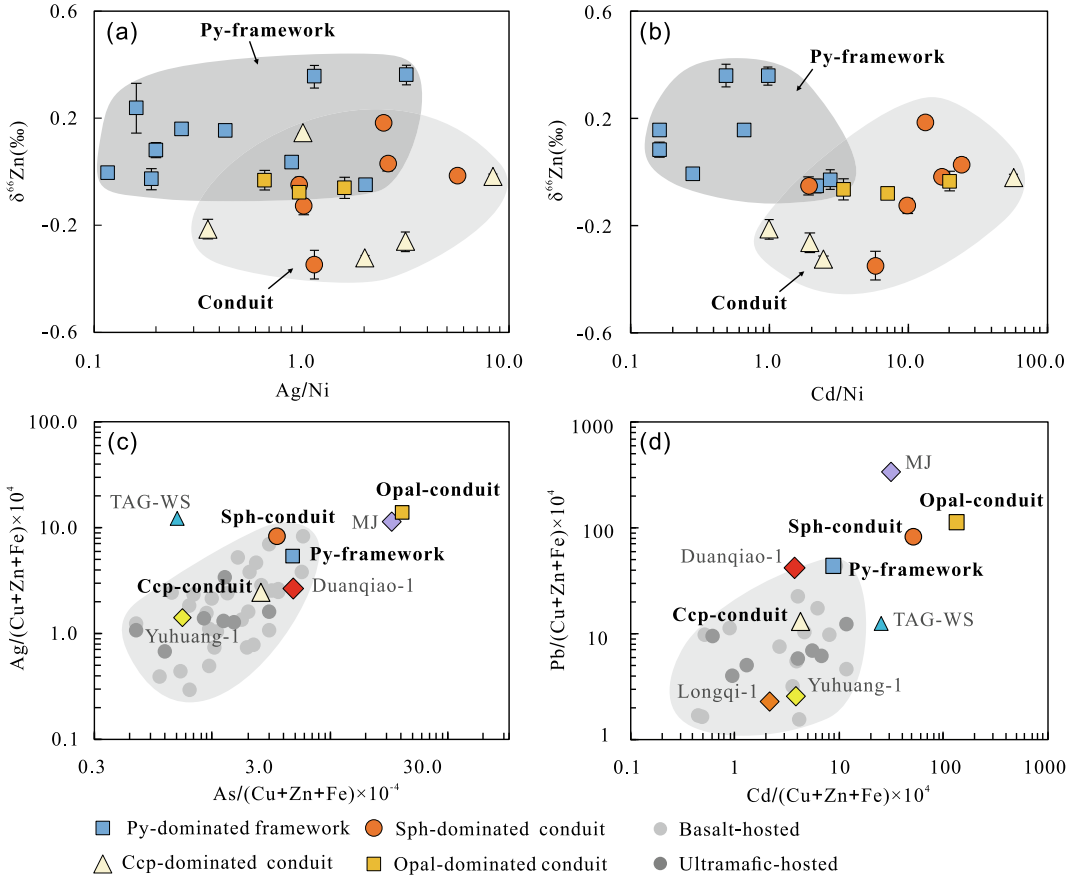

Fig. 5. Diagrams showing the (a) higher Ag/Ni and (b) Cd/Ni ratios but isotopically lighter Zn within the conduit samples. The (c) As and Ag and (d) Cd and Pb to Cu + Zn + Fe content ratios showing enrichment of these elements in the studied sulfide samples from DHF compared with mafic- and ultramafic-hosted hydrothermal fields on mid-ocean ridges (Hannington et al., 2005; Fouquet et al., 2010 and references therein). The element ratios of bulk sulfide in Duanqiao-1 (Yang, 2017) are also shown. Data base: Longqi-1 (Tao et al., 2011); Mount Jourdanne (MJ; Nayak et al., 2014); TAG-white smoker (TAG-WS; Tivey et al., 1995); Yuhuang-1 (Liao et al., 2018).

+4.71 ‰), because sulfur fractionation between chalcopyrite and the parent fluid H_2S is negligible ($\delta^{34}S_{Cpy\text{-}H2S}$ = −0.1 ‰ at 350 °C; Ohmoto, 1979). The Zn isotope composition is calculated as $\delta^{66}Zn_{final\ fluid}$ = +0.18 ‰, based on a fractionation factor ($\alpha_{ZnS\text{-}Sol.}$) of 0.9997 and the $\delta^{66}Zn$ value of the chalcopyrite-rich conduit samples (averaged −0.09 ‰; Table 1).

Therefore, the extent of the subsurface remobilization was estimated by the coupled Zn and S isotope compositions of the studied sulfide samples, as shown in the following equations:

$$a \times \delta^{66}Zn_{leachate} + b \times \delta^{66}Zn_{initial\ fluid} + c \times \delta^{66}Zn_{seawater} = \delta^{66}Zn_{final\ fluid}, \quad (1)$$

$$a \times \delta^{34}S_{leachate} + b \times \delta^{34}S_{initial\ fluid} + c \times \delta^{34}S_{seawater} = \delta^{34}S_{final\ fluid}, \quad (2)$$

and

$$a + b + c = 1, \quad (3)$$

where a, b, and c represent the ratio of leachate, initial hydrothermal fluid, and seawater, respectively.

Based on the above equations and input values, the leachate component (a) is calculated as 29.5 %-67.2 %, while the values for seawater(c) ranging between 5.8 and 12.9 %. These results indicate that the remobilized Zn comprise about 1/3 to 2/3 of the total Zn in the final hydrothermal fluid. Moreover, the lowest $\delta^{66}Zn_{final\ precipitates}$ value of the conduit sulfide samples (down to −0.35 ‰) is lower than the value of the precipitates from the assumed leachate ($\delta^{66}Zn_{leachate}$ = −0.32 ‰ to −0.17 ‰). Thus, we propose that the light Zn isotope compositions (down to −0.35 ‰) of the conduit samples likely reflect recurring leaching of isotopically light sub-seafloor sulfides. This interpretation is consistent with dating results showing at least four episodes of hydrothermal activity may have occurred at the vent field (Yang et al., 2016).

5.4. Isotopic constraints on the hydrothermal Zn flux to the ocean

Distinct Zn isotope compositions are observed in the sulfide framework and conduit samples, interpreted here as derived from the remobilization of sub-seafloor sulfide minerals. Intensive Zn isotope fractionation features and significant negative $\delta^{66}Zn$ values have been observed in many seafloor hydrothermal fields located on sediment-starved MORs (Fig. 4b). For example, $\delta^{66}Zn$ values of −0.43 ‰ from Yuhuang-1 on the SWIR (Liao et al., 2019), −0.39 ‰ from the Edmond field on the Central Indian Ridge (Wu, et al., 2013; Zeng et al., 2021), and −0.14 ‰ from the south Mid-Atlantic ridge (Li et al., 2018) have been reported. Measured $\delta^{66}Zn$ values as low as −0.43 ‰ were also reported from stockwork mineralization in the Alexandrinka VMS deposit (Mason et al., 2005). These $\delta^{66}Zn$ values are all significantly lower than those of precipitates (lowest value about −0.05 ‰, fractionation factor ($\alpha_{ZnS\text{-}Sol.}$) of 0.9997) from the initial hydrothermal fluids formed by the reaction of seawater with basement rocks (+0.24 ‰; John et al., 2008). Negative $\delta^{66}Zn$ values (−0.5 ‰) were also recorded from the hydrothermal plume above the TAG active mound

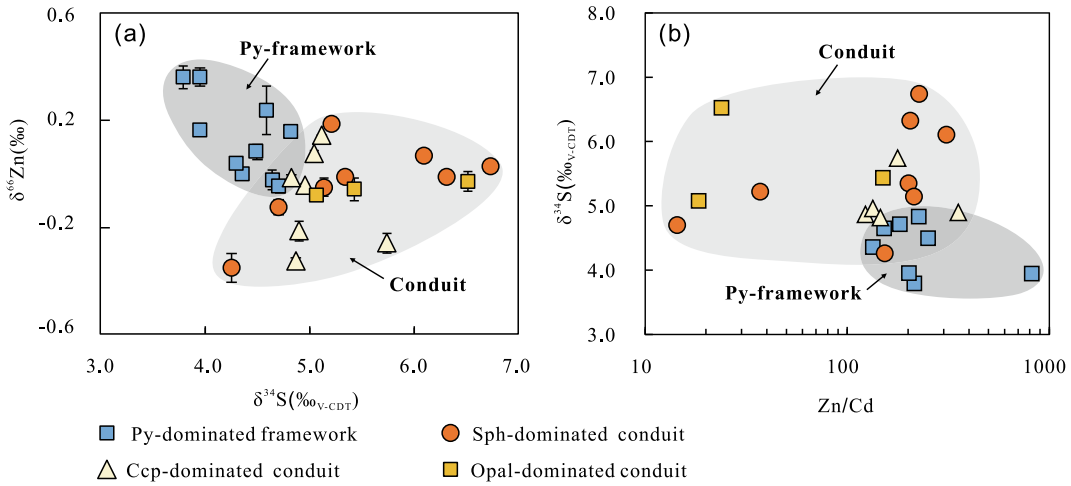

Fig. 6. (a) δ^{66}Zn vs δ^{34}S diagram showing the heavier Zn and lighter S of the pyrite-dominated framework compared with those of the conduit samples. (b) No correlation is observed between the Zn/Cd ratio and δ^{66}Zn values, implying that decreasing temperature was not the main factor controlling the Zn isotope fractionation.

(Conway and John, 2014), and hydrothermal vents along the Reykjanes Ridge (−0.42 ‰; Lemaitre et al., 2020). We suggest that while hydrothermal mineral precipitation is expected to generate late-stage precipitates with heavier Zn (Fig. 7); but, because of the relatively simple source of Zn in sediment-starved MOR hydrothermal systems, the negative values also probably resulted from subsurface remobilization and re-precipitation. This interpretation is also consistent with the finding that hydrothermal fields found on slow- and ultraslow-spreading ridges exhibit relatively low δ^{66}Zn values with a large distribution range (Fig. 4b), due to long-lived hydrothermal activity occurring in stable, longer-lived tectonic settings; than those of fast spreading ridges. Thus, our study reflects that subsurface remobilization is likely a common phenomenon in hydrothermal fields on MORs, particularly on slow- and ultraslow-spreading ridges.

Previous studies have revealed that the Zn isotopic composition of seawater (δ^{66}Zn = +0.46 ± 0.13 ‰) is heavier than other postulated Zn inputs (e.g., rivers; δ^{66}Zn = +0.33 ‰, and aeolian dust; δ^{66}Zn = +0.37 ± 0.14 ‰), while outputs in oxic settings, such as deep-sea clay, surface sediments, manganese nodules, and biogenic opal are generally isotopically heavier than seawater (Fig. 8). These inputs and outputs require an isotopically light Zn sink of 3.1 × 10^8 mol/year with a δ^{66}Zn value of −0.3 ‰ (Little et al., 2014). A possible isotopically light Zn sink is organic-rich continental margin sediments (5.6 × 10^8 mol/year, average δ^{66}Zn = −0.09 ‰ to +0.12 ‰; Little et al., 2016; Zhang et al., 2021), that contain isotopically light Zn that is bounded by organic matters (Fan et al., 2018; Weber et al., 2018), or incorporated into authigenic oxides or sulfides (Vance et al., 2016; Zhang et al., 2021).

Although the majority of Zn in hydrothermal fluids precipitates immediately after fluid venting, recent studies suggest that significant amounts of Zn can be dispersed in hydrothermal plumes as either particles or in dissolved forms at up to basin-scale distances (German et al., 1991; Roshan et al., 2016; Lemaitre et al., 2020). For example, particulate Zn accounts for about 85 ± 23 % of the total Zn in buoyant plumes at the Aisics site (Waeles et al., 2017), and significant particulate Zn concentrations have been observed in hydrothermal plumes among hydrothermal fields on a variety of ridge systems (Edmonds and German, 2004; Sun et al., 2014; John et al., 2018; Lemaitre et al., 2020). In addition to negative δ^{66}Zn values identified in hydrothermal plume in slow-ultraslow spreading ridges (Conway and John, 2014; Lemaitre et al., 2020), our study reveals that hydrothermal Zn may be even lighter than

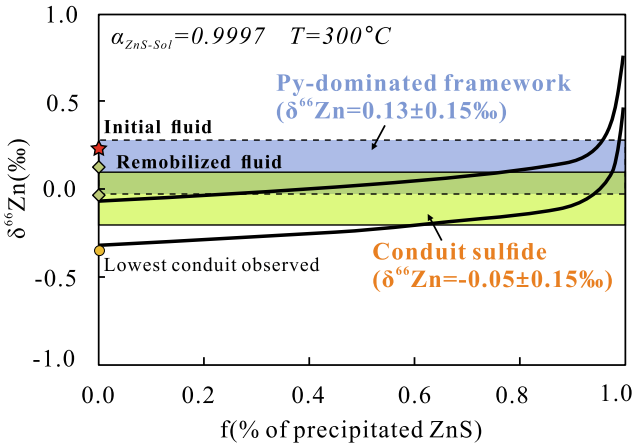

Fig. 7. Rayleigh fractionation modeling of Zn isotope values for sphalerite precipitated from the hydrothermal fluids. The assumed fractionation factor ($\alpha_{ZnS\text{-}Sol}$) between sphalerite and solution is 0.9997 (Jamieson-Hanes et al., 2017). The red star indicates the assumed initial fluid composition. Green diamonds show the range of remobilized fluid compositions; see details in the text. The observed lowest δ^{66}Zn value of the conduit sulfide samples is lower than the proposed lowest value precipitated from the remobilized fluid.

previously estimated (δ^{66}Zn = +0.2 ‰; John et al., 2008) due to the process of subsurface remobilization, thus increasing the size of the previously identified isotopically light Zn sink required to balance the global oceanic zinc budget.

To date, estimates of the Zn flux in hydrothermal plumes on MORs vary by orders of magnitude. The global oceanic hydrothermal Zn flux, is estimated to be about 1.2–3.2 × 10^9 mol/year (Elderfield and Schultz, 1996), provides about 1.2–3.2 × 10^8 mol/year of Zn to plumes based on about 90 % of the Zn being deposited adjacent to the field. However, more recent estimates suggest that the effective hydrothermal Zn flux in a plume may be underestimated, and that the global oceanic hydrothermal flux of dissolved Zn into the ocean may be up to 1.75 ± 0.35 × 10^9 mol/year (Roshan et al., 2016). The above mentioned light sink of continental margin sediments was found to only accommodate the lower end of the estimated hydrothermal Zn input (0.4–2.8 × 10^9 mol/year; Roshan et al., 2018). Based on slow-ultraslow spreading ridges constituting about 60 % of the length of the total ridge systems, their associate hydrothermal Zn flux could be roughly estimated to be about 1.05 × 10^9mol/year. Assuming 29.5 %-67.2 % of the Zn being of remobilized origin with a δ^{66}Zn value of −0.05 ‰, as in Duanqiao-1 (Fig. 8),

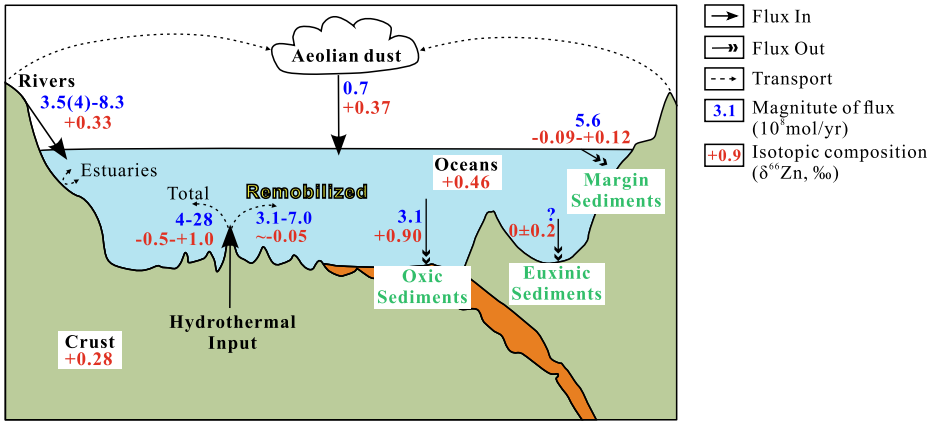

Fig. 8. Diagram of the δ^{66}Zn isotopic mass balance, indicating remobilized Zn on slow-ultraslow spreading ridges may be an important light Zn isotope composition input to the ocean, modified after Little et al. (2014). Data base: continental margin sediment (Little et al, 2016), euxinic sediments (Vance et al., 2016), and zinc flux of total hydrothermal input (Roshan et al., 2016, 2018), δ^{66}Zn values of seawater (Lemaitre et al., 2020), crust (Wang et al., 2017), and total hydrothermal input (John et al., 2008; Conway and John, 2014; Lemaitre et al., 2020), remobilized fluid (this study). The pink symbols indicate Zn inputs, while the green symbols represent possible outputs.

the size of previously identified isotopically light Zn sink would be 3.6×10^8 –4.3×10^8 mol/year, with a δ^{66}Zn value of −0.3 ‰. This value is 15 %-40 % larger than the previously estimated flux (3.1×10^8 mol/year with a δ^{66}Zn value of −0.3 ‰). Furthermore, more intensive remobilization is implied because the δ^{66}Zn values arising from remobilized Zn, such as the observations of plumes at TAG and along the Reykjanes Ridge (Conway and John, 2014; Lemaitre et al., 2020), is even lighter than those measured in this study, implying that the recalculated value may be even larger.

6. Conclusion

(a) Sulfide samples recovered from the DHF on the SWIR exhibit δ^{66}Zn values ranging between −0.35 ‰ and +0.36 ‰. For the first time, hand-specimen-scale seafloor hydrothermal field late-stage conduit samples are observed to have lighter Zn isotope compositions (−0.35 ‰ to +0.18 ‰) than early-stage pyrite-dominated framework samples (−0.05 ‰ to +0.36 ‰).

(b) This isotopic distribution is interpreted to result from the remobilization of subsurface mineralization, which is consistent with Pb, As, Cd, and Ag enrichment and heavier S isotope compositions within the sulfide minerals of the conduit samples. Based on endmember isotope compositions, remobilized Zn was calculated making up about 1/3 to 2/3 of the total Zn content in the final-stage hydrothermal fluid that formed the conduit samples.

(c) Subsurface remobilization is likely a common feature during the formation of seafloor sulfides, and it may significantly increase the magnitude of the light zinc sink needed to balance the oceanic isotope mass balance.

Data availability

The data has been attached in "Supplementary material".

Declaration of Competing Interest

The authors declare that they have no known competing financial interests or personal relationships that could have appeared to influence the work reported in this paper.

Acknowledgment

This research was funded by the Scientific Research Fund of the Second Institute of Oceanography, Ministry of Natural Resources (JG1905), National Natural Science Foundation of China (92162214, 42006074, 42073010, 41773015, U1812402), Natural Science Foundation of Zhejiang Province (LQ19D060002), National Key Research and Development Program of China (2018YFC0309902), China Ocean Mineral Resources R & D Association Project (DY135-S1-1-02), Macao Science and Technology Development Fund (No. FDCT 0041/2021/A1), and Key Research and Development Program of Yunan Province (202103AQ100003). We would like to thank the captains and crews who contributed to the success of this project. We are also grateful for the constructive comments and suggestions from editor Tim Conway, Andy Heard and another two anonymous reviewers. We thank Duncan Miers for revising the English of the last version of the manuscript.

Appendix A. Supplementary material

Supplementary material to this article can be found online at https://doi.org/10.1016/j.gca.2022.08.022.

References

Archer, C., Andersen, M.B., Cloquet, C., Conway, T.M., Dong, S., Ellwood, M., Moore, R., Nelson, J., Rehkämper, M., Rouxel, O., Samanta, M., Shin, K., Sohrin, Y., Takano, S., Wasylenki, L., 2017. Inter-calibration of a proposed new primary reference standard AA-ETH Zn for zinc isotopic analysis. J. Anal. Atom. Spectrom. 32, 415–419.

Bluth, G.J., Ohmoto, H., 1988. Sulfide-sulfate chimneys on the East Pacific Rise, 11° and 13°N latitudes. Part II: Sulfur isotopes. Can. Mineral. 26, 487–504.

Chen, J.B., Gaillardet, J., Dessert, C., Villemant, B., Louvat, P., Crispi, O., et al., 2014. Zn isotope compositions of the thermal spring waters of La Soufrière volcano, Guadeloupe Island. Geochim. Cosmochim. Acta 127, 67–82.

Cherkashov, G., Kuznetsov, V., Kuksa, K., Tabuns, E., Maksimov, F., Bel'Tenev, V., 2017. Sulfide geochronology along the Northern Equatorial Mid-Atlantic Ridge. Ore Geol. Rev. 87, 147–154.

Conway, T.M., John, S.G., 2014. The biogeochemical cycling of zinc and zinc isotopes in the North Atlantic Ocean. Global Biogeochem. Cy. 28, 1111–1128.

Dick, H.J., Lin, J., Schouten, H., 2003. An ultraslow-spreading class of ocean ridge. Nature 426, 405–412.

Dong, S.F., Chen, D.Z., Qing, H.R., Jiang, M.S., Zhou, X.Q., 2013. In situ stable isotopic constraints on dolomitizing fluids for the hydrothermally-originated saddle dolomites at Keping, Tarim Basin. Chin. Sci. Bull. 58, 2877–2882.

Edmonds, H.N., German, C.R., 2004. Particle geochemistry in the Rainbow hydrothermal plume, Mid-Atlantic Ridge. Geochim. Cosmochim. Acta 68, 759–772.

Elderfield, H., Schultz, A., 1996. Mid-ocean ridge hydrothermal fluxes and the chemical composition of the ocean. Annu. Rev. Earth Pl. Sc. 24, 191–224.
Fan, H.F., Wen, H.J., Xiao, C.Y., Zhou, T., Cloquet, C., Zhu, X.K., 2018. Zinc geochemical cycling in a Phosphorus-rich Ocean during the early Ediacaran. J. Geophys. Res. Oceans 123, 5248–5260.
Fernandez, A., Borrok, D.M., 2009. Fractionation of Cu, Fe, and Zn isotopes during the oxidative weathering of sulfide-rich rocks. Chem. Geol. 264, 1–12.
Fouquet, Y., Cambon, P., Etoubleau, J., Charlou, J.L., Ondréas, H., Barriga, F.J., Cherkashov, G., Semkova, T., Poroshina, I., Bohn, M., Donval, J.P., Henry, K., Murphy, P., Rouxel, O., 2010. Geodiversity of hydrothermal processes along the Mid-Atlantic Ridge–Ultramafic-hosted mineralization: A new type of oceanic Cu-Zn-Co-Au volcanogenic massive sulfide deposit. In: Rona, P.A., Devey, C.W., Dyment, J., Murton, B.J. (Eds.), Diversity of Hydrothermal Systems on Slow Spreading Ocean Ridges. American Geophysical Union, Washington DC, pp. 321–367.
Fujii, T., Moynier, F., Pons, M., Albarède, F., 2011. The origin of Zn isotope fractionation in sulfides. Geochim. Cosmochim. Acta. 75, 7632–7643.
George, L., Cook, N., Crowe, B., Ciobanu, C., 2018. Trace elements in hydrothermal chalcopyrite. Mineral. Mag. 82, 59–88.
Georgen, J.E., Lin, J., Dick, H.J.B., 2001. Evidence from gravity anomalies for interactions of the Marion and Bouvet hotspots with the Southwest Indian Ridge: Effects of transform offsets. Earth Planet. Sc. Lett. 187, 283–300.
German, C.R., Campbell, A.C., Edmond, J.M., 1991. Hydrothermal scavenging at the Mid-Atlantic Ridge: Modification of trace element dissolved fluxes. Earth Planet. Sc. Lett. 107, 101–114.
Grevemeyer, I., Hayman, N., Lange, D., Peirce, C., Papenberg, C., Van Avendonk, H., Schmid, F., Gómez De La Peña, L., Dannowski, A., 2019. Constraining the maximum depth of brittle deformation at slow- and ultraslow-spreading ridges using microseismicity. Geology 47, 1069–1073.
Hannington, M.D., de Ronde, C.D., Petersen, S., 2005. Sea-floor tectonics and submarine hydrothermal systems. Econ. Geol. 100, 111–141.
Huang, J., Liu, S.A., Gao, Y.J., Xiao, Y.L., Chen, S., 2016. Copper and zinc isotope systematics of altered oceanic crust at IODP Site 1256 in the eastern equatorial Pacific. J. Geophys. Res.: Solid Earth 121, 7086–7100.
Isson, T.T., Love, G.D., Dupont, C.L., Reinhard, C.T., Zumberge, A.J., Asael, D., Gueguen, B., Mccrow, J., Gill, B.C., Owens, J., Rainbird, R.H., Rooney, A.D., Zhao, M., Stueeken, E.E., Konhauser, K.O., John, S.G., Lyons, T.W., Planavsky, N.J., 2018. Tracking the rise of eukaryotes to ecological dominance with zinc isotopes. Geobiology 16, 341–352.
Jamieson-Hanes, J.H., Shrimpton, H.K., Veeramani, H., Ptacek, C.J., Lanzirotti, A., Newville, M., Blowes, D.W., 2017. Evaluating zinc isotope fractionation under sulfate reducing conditions using a flow-through cell and in situ XAS analysis. Geochim. Cosmochim. Acta 203, 1–14.
Jian, H.C., Singh, S.C., Chen, Y.J., Li, J.B., 2017. Evidence of an axial magma chamber beneath the ultraslow-spreading Southwest Indian Ridge. Geology 45, G38351–G38356.
John, S.G., Rouxel, O.J., Craddock, P.R., Engwall, A.M., Boyle, E.A., 2008. Zinc stable isotopes in seafloor hydrothermal vent fluids and chimneys. Earth Planet. Sc. Lett. 269, 17–28.
John, S.G., Helgoe, J., Townsend, E., 2018. Biogeochemical cycling of Zn and Cd and their stable isotopes in the Eastern Tropical South Pacific. Mar. Chem. 201, 256–262.
Keith, M., Haeckel, F., Haase, K.M., Schwarz-Schampera, U., Klemd, R., 2016. Trace element systematics of pyrite from submarine hydrothermal vents. Ore Geol. Rev. 72, 728–745.
Kelley, K.D., Wilkinson, J.J., Chapman, J.B., Crowther, H.L., Weiss, D.J., 2009. Zinc isotopes in sphalerite from base metal deposits in the Red Dog district, northern Alaska. Econ. Geol. 104, 767–773.
Lemaitre, N., de Souza, G.F., Archer, C., Wang, R., Planquette, H., Sarthou, G., Vance, D., 2020. Pervasive sources of isotopically light zinc in the North Atlantic Ocean. Earth Planet. Sc. Lett. 539, 116216.
Li, J.B., Jian, H.C., Chen, Y.S.J., Singh, S.C., Ruan, A., Qiu, X.L., Zhao, M.H., Wang, X.G., Niu, X.G., Ni, J.Y., Zhang, J.Z., 2015. Seismic observation of an extremely magmatic accretion at the ultraslow spreading Southwest Indian Ridge. Geophys. Res. Lett. 42 (8), 2656–2663.
Li, X.H., Wang, J.Q., Chu, F.Y., Lei, J.J., Wang, H., Li, Z.G., 2018. Zn isotopes in hydrothermal sulfides and their oxidation products along the south mid-Atlantic ridge evidence of hydrothermal fluid deposition. Geo-Mar. Lett. 38, 131–138.
Liao, S.L., Tao, C.H., Li, H.M., Barriga, F.J.A.S., Liang, J., Yang, W.F., Yu, J.Y., Zhu, C.W., 2018. Bulk geochemistry, sulfur isotope characteristics of the Yuhuang-1 hydrothermal field on the ultraslow-spreading Southwest Indian Ridge. Ore Geol. Rev. 96, 13–27.
Liao, S.L., Tao, C.H., Zhu, C.W., Li, H.M., Li, X.H., Liang, J., Yang, W.F., Wang, Y.J., 2019. Two episodes of sulfide mineralization at the Yuhuang-1 hydrothermal field on the Southwest Indian Ridge: Insight from Zn isotopes. Chem. Geol. 507, 54–63.
Little, S.H., Vance, D., Walker-Brown, C., Landing, W.M., 2014. The oceanic mass balance of copper and zinc isotopes, investigated by analysis of their inputs, and outputs to ferromanganese oxide sediments. Geochim. Cosmochim. Acta 125, 673–693.
Little, S.H., Vance, D., Mcmanus, J., Severmann, S., 2016. Key role of continental margin sediments in the oceanic mass balance of Zn and Zn isotopes. Geology 44, G37491–G37493.
Liu, S.A., Liu, P.P., Lv, Y.W., Wang, Z.Z., Dai, J.G., 2019. Cu and Zn isotope fractionation during oceanic alteration: Implications for Oceanic Cu and Zn cycles. Geochim. Cosmochim. Acta 257, 191–205.
Mason, T.F., Weiss, D.J., Chapman, J.B., Wilkinson, J.J., Tessalina, S.G., Spiro, B., Horstwood, M.S., Spratt, J., Coles, B.J., 2005. Zn and Cu isotopic variability in the Alexandrinka volcanic-hosted massive sulphide (VHMS) ore deposit, Urals, Russia. Chem. Geol. 221, 170–187.
Nayak, B., Halbach, P., Pracejus, B., Münch, U., 2014. Massive sulfides of Mount Jourdanne along the super-slow spreading Southwest Indian Ridge and their genesis. Ore Geol. Rev. 63, 115–128.
Ohmoto, H., 1972. Systematics of sulfur and carbon isotopes in hydrothermal ore deposits. Econ. Geol. 67, 551–578.
Ohmoto, H., 1979. Isotopes of sulfur and carbon. Geochem. Hydrothermal Ore Depos., 509–567
Petersen, S., Herzig, P.M., Hannington, M.D., 2000. Third dimension of a presently forming VMS deposit: TAG hydrothermal mound, Mid-Atlantic Ridge, 26 ° N. Miner. Deposita 35, 233–259.
Reich, M., Deditius, A., Chryssoulis, S., Li, J.W., Ma, C.Q., Parada, M.A., Barra, F., Mittermayr, F., 2013. Pyrite as a record of hydrothermal fluid evolution in a porphyry copper system: A SIMS/EMPA trace element study. Geochim. Cosmochim. Acta 104, 42–62.
Roshan, S., Wu, J., Jenkins, W.J., 2016. Long-range transport of hydrothermal dissolved Zn in the tropical South Pacific. Mar. Chem. 183, 25–32.
Roshan, S., Devries, T., Wu, J., Chen, G., 2018. The internal cycling of zinc in the ocean. Global Biogeochem. Cy. 32, 1833–1849.
Sarrazin, J., Juniper, S.K., Massoth, G., Legendre, P., 1999. Physical and chemical factors influencing species distributions on hydrothermal sulfide edifices of the Juan de Fuca Ridge, northeast Pacific. Mar. Ecol. Prog. Ser. 190, 89–112.
Sauter, D., Cannat, M., Meyzen, C., Bezos, A., Patriat, P., Humler, E., Debayle, E., 2009. Propagation of a melting anomaly along the ultraslow Southwest Indian Ridge between 46°E and 52°20′E: Interaction with the Crozet hotspot? Geophys. J. Int. 179, 687–699.
Schenke, H., 2016. General Bathymetric Chart of the Oceans (GEBCO). In: Harff, J., Meschede, M., Petersen, S., Thiede, J. (Eds.), Encyclopedia of Marine Geosciences. Encyclopedia of Earth Sciences Series. Springer, Dordrecht.
Schwartz, M.O., 2000. Cadmium in zinc deposits: Economic geology of a polluting element. Int. Geol. Rev. 42, 445–469.
Shanks, W.C., 2001. Stable isotopes in seafloor hydrothermal systems: Vent fluids, hydrothermal deposits, hydrothermal alteration, and microbial processes. Rev. Mineral. Geochem. 43, 469–525.
Shanks III, W.C., Seyfried Jr, W.E., 1987. Stable isotope studies of vent fluids and chimney minerals, southern Juan de Fuca Ridge: Sodium metasomatism and seawater sulfate reduction. J. Geophys. Res.: Atmos. 92, 11387–11399.
Sun, X.X., Yang, Z.S., Fan, D.J., Liu, M., 2014. Suspended zinc sulfide particles in the Southwest Indian Ridge area and their relationship with hydrothermal activity. Chin. Sci. Bull. 59, 913–923.
Syverson, D.D., Ono, S., Shanks, W.C., Seyfried, W.E., 2015. Multiple sulfur isotope fractionation and mass transfer processes during pyrite precipitation and recrystallization: An experimental study at 300 and 350°C. Geochim. Cosmochim. Acta. 165, 418–434.
Tao, C.H., Li, H.M., Huang, W., Han, X.Q., Wu, G.H., Su, X., Zhou, N., Lin, J., He, Y.H., Zhou, J.P., 2011. Mineralogical and geochemical features of sulfide chimneys from the 49°39′ E hydrothermal field on the Southwest Indian Ridge and their geological inferences. Chin. Sci. Bull. 56, 2828–2838.
Tao, C.H., Li, H.M., Jin, X.B., Zhou, J.P., Wu, T., He, Y.H., Deng, X.M., Gu, C.H., Zhang, G. Y., Liu, W.O., 2014. Seafloor hydrothermal activity and polymetallic sulfide exploration on the southwest Indian ridge. Chin. Sci. Bull. 59, 2266–2276.
Tao, C.H., Lin, J., Guo, S.Q., Chen, John, Wu, G.H., Han, X.Q., German, C.R., Yoerger, D. R., Zhou, N., Li, H.M., Su, X., Zhu, J., 2012. First active hydrothermal vents on an ultraslow-spreading center: Southwest Indian Ridge. Geology 40, 47–50.
Tivey, M.K., 2007. Generation of seafloor hydrothermal vent fluids and associated mineral deposits. Oceanography 20, 50–65.
Tivey, M.K., Humphris, S.E., Thompson, G., Hannington, M.D., Rona, P.A., 1995. Deducing patterns of fluid-flow and mixing within the TAG active hydrothermal mound using mineralogical and geochemical data. J. Geophys. Res.: Solid Earth 100, 12527–12555.
Tostevin, R., Turchyn, A.V., Farquhar, J., Johnston, D.T., Eldridge, D.L., Bishop, J.K.B., Mcilvin, M., 2014. Multiple sulfur isotope constraints on the modern sulfur cycle. Earth Planet. Sc. Lett. 396, 14–21.
Vance, D., Little, S.H., Archer, C., Cameron, V., Andersen, M.B., Rijkenberg, M.J.A., Lyons, T.W., 2016. The oceanic budgets of nickel and zinc isotopes: The importance of sulfidic environments as illustrated by the Black Sea. Philos. Trans. R. Soc. London, Ser. A. 374, 20150294.
Waeles, M., Cotte, L., Pernet-Coudrier, B., Chavagnac, V., Cathalot, C., Leleu, T., Laes-Huon, A., Perhirin, A., Riso, R.D., Sarradin, P., 2017. On the early fate of hydrothermal iron at deep-sea vents: A reassessment after in situ filtration. Geophys. Res. Lett. 44, 4233–4240.
Wang, M., Cai, F., Li, Q., Liang, J., Yan, G.I., Dong, G., Wang, F., Shao, H.B., Hu, G.W., 2015. Characteristics of authigenic pyrite and its sulfur isotopes influenced by methane seep at Core a, Site 79 of the middle Okinawa Trough. Sci. China Earth Sci. 58, 2145–2153.
Wang, Z.Z., Liu, S.A., Liu, J.G., Huang, J., Xiao, Y., Chu, Z.Y., Zhao, X.M., Tang, L.M., 2017. Zinc isotope fractionation during mantle melting and constraints on the Zn isotope composition of Earth's upper mantle. Geochim. Cosmochim. Acta 198, 151–167.
Weber, T., John, S., Tagliabue, A., Devries, T., 2018. Biological uptake and reversible scavenging of zinc in the global ocean. Science 361, 72–76.

Wen, H.J., Zhu, C.W., Zhang, Y.X., Cloquet, C., Fan, H.F., Fu, S.H., 2016. Zn/Cd ratios and cadmium isotope evidence for the classification of lead-zinc deposits. Sci. Rep. 6, 25273.

Woodruff, L.G., Shanks III, W.C., 1988. Sulfur isotope study of chimney minerals and vent fluids from 21°N, East Pacific Rise: Hydrothermal sulfur sources and disequilibrium sulfate reduction. J. Geophys. Res.: Atmos. 93, 4562–4572.

Wu, Z.W., Sun, X.M., Wang, Y., Liang, Y.H., Xu, L., 2013. Preliminary study of Fe-Cu-zinc isotope characteristics of polymetallic sulfide in the Centrial Indian Ridge. Acta Mineralogica Sinica S2, 672–673 (In Chinese with English abstract).

Yang, W.F., 2017. Study of hydrothermal mineralization of Duanqiao hydrothermal field in Southwest Indian Ridge. Ph. D. thesis, Zhejiang University. (In Chinese with English abstract).

Yang, Z., Song, W.R., Wen, H.J., Zhang, Y.X., Fan, H.F., Wang, F., Li, Q.K., Yang, T., Zhou, Z.B., Liao, S.L., Zhu, C.W., 2022a. Zinc, cadmium and sulphur isotopic compositions reveal biological activity during formation of a volcanic-hosted massive sulphide deposit. Gondwana Res. 101, 103–113.

Yang, W.F., Tao, C.H., Li, H.M., Liang, J., Liao, S.L., Long, J.P., Ma, Z.B., Wang, L.S., 2016. $^{230}Th/^{238}U$ dating of hydrothermal sulfides from Duanqiao hydrothermal field, Southwest Indian Ridge. Mar. Geophys. Res. 38, 1–13.

Yang, W.F., Liao, S.L., Dias, Á., Liang, J., Li, W., Ding, T., Tao, C.H., 2022. Geochemistry, sulfur and lead isotopic composition of hydrothermal sulfide from the Duanqiao hydrothermal field on the Southwest Indian Ridge: Implications for ore genesis. *Int. Geol. Rev*. doi: 10.1080/00206814.2022.2081937.

Yang, A.Y., Zhao, T.P., Zhou, M.F., Deng, X.G., 2017. Isotopically enriched N-MORB: A new geochemical signature of off-axis plume-ridge interaction-A case study at 50°28'E, Southwest Indian Ridge. J. Geophys. Res. 122, 191–213.

Yu, X., Dick, H.J.B., 2020. Plate-driven micro-hotspots and the evolution of the Dragon Flag melting anomaly, Southwest Indian Ridge. Earth Planet. Sc. Lett. 531, 116002.

Zeng, Z.G., Ma, Y., Chen, S., Selby, D., Wang, X.Y., Yin, X.B., 2017. Sulfur and lead isotopic compositions of massive sulfides from deep-sea hydrothermal systems: Implications for ore genesis and fluid circulation. Ore Geol. Rev. 87, 155–171.

Zeng, Z.G., Li, X.H., Chen, S., de Jong, J., Mattielli, N., Qi, H., Pearce, C., Murton, B.J., 2021. Iron, copper, and zinc isotopic fractionation in seafloor basalts and hydrothermal sulfides. Mar. Geol. 436, 106491.

Zhang, B.S., Li, Z.Q., Hou, Z.Q., Zhang, W.Y., Xu, B., 2018. Mineralogy and chemistry of sulfides from the Longqi and Duanqiao hydrothermal fields in the Southwest Indian Ridge. Acta Geol. Sin. 92, 1798–1822.

Zhang, Y.Y., Planavsky, N.J., Zhao, M.Y., Isson, T., Asael, D., Wang, C.L., Wang, F., 2021. The isotopic composition of sedimentary organic zinc and implications for the global Zn isotope mass balance. Geochim. Cosmochim. Acta. 314, 16–26.

Zhang, X., Zhai, S.K., Yu, Z.H., Yang, Z.F., Xu, J., 2019. Zinc and lead isotope variation in hydrothermal deposits from the Okinawa Trough. Ore Geol. Rev., 102944

Zhou, J.X., Huang, Z.L., Zhou, M.F., Zhu, X.K., Muchez, P., 2014. Zinc, sulfur and lead isotopic variations in carbonate-hosted Pb–Zn sulfide deposits, Southwest China. Ore Geol. Rev. 58, 41–54.

Zhu, C.W., Liao, S.L., Wang, W., Zhang, Y.X., Yang, T., Fan, H.F., Wen, H.J., 2018. Variations in Zn and S isotope chemistry of sedimentary sphalerite, Wusihe Zn-Pb deposit, Sichuan Province, China. Ore Geol. Rev. 95, 639–648.